CHAPTER 5

EFFECT OF LITHIUM ION CONCENTRATION ON LUMINESCENCE AND FERROMAGNETIC PROPERTIES OF EUROPIUM DOPED ZINC OXIDE NANOPARTICLES

5.1. INTRODUCTION

In the previous chapters, transition metal doped ZnO have been synthesized and characterized to study its properties as well as their influence on properties of ZnO. This chapter describes the effect of rare earth (Eu) ions co-doped with Li on structural optical and magnetic properties of ZnO. Lanthanides doped semiconductors are materials of paramount importance due to their potential applications in optoelectronic devices, X-ray imaging, flat panel display, optical communication, biological labels and scintillator [138-139]. Lanthanides show sharp and intense emission band in visible region by ultraviolet light/visible irradiation, which are originated from intermolecular *f-f* transition. On account of its valuable technological interest, many studies have been devoted to lanthanides doped semiconductors. The scientific fraternity around the world exploring wide range applications of diluted magnetic semiconductor (DMS) as solar cell, chemical sensors, and spintronics applications [140]. The advantage of using lanthanides ions activator at crystallographic site of DMS are that, we get promising visible luminescent properties coupled with unique qualities of the semiconductors.

The high thermal, chemical, mechanical stability and bio-compatibility made ZnO, one of the most suitable host material for different rare earth and transition metal doping. Diluted magnetic semiconductors nanorods, quantum dot, nanowires, nanotubes, nanobelts, naocombs, nanoring, nanospring, nanopropellers, nanosheets, nanodrums and tetra pods-like nanostructure are of crucial interest for new technologies [141]. However, despite the widespread technological interest in different semiconductor, zinc oxide is still a promising

host. Its integration with other materials (transition metal and rare earth) explores new and improved applications. The incorporation of dopant ions in zinc oxide causes, shift in absorption edge, creates defect level absorption in visible region, enhances its visible luminescence and changes its RTFM properties [142-143].

The lanthanides materials have bright luminescence in visible region. The intense red emission of europium, green emission of terbium and yellow emission of dysprosium can be attributed to electronic structure of the lanthanides ions, and the *f-f* transitions. By using one or more than one lanthanide doping the luminescence properties can be tailored towards emission at selective wavelengths. These unique properties of rare earth triggered a number of studies on rare earth doped ZnO. Zinc oxide has emission in violet colour and rare earths are well known for their luminescence properties. Therefore much attention has been paid for luminescence enhancement by rare earth doping in zinc oxide, while very few studies have been done on magnetic properties of rare earth doped ZnO. RTFM has been observed in pure as well as doped oxides. The presence of RTFM in pure oxide is even questionable due to absence of magnetic ions. The origin of ferromagnetism in pure and doped zinc oxides remains controversial. The scientific fraternity has explained it by diverse prospective such as oxygen vacancies, oxygen interstitial, Zn vacancies and Zn interstitial [144-145]. Our earlier discussion in chapter 3 and chapter 4 suggest that defect in the system significantly affects the magnetic property of Co doped ZnO and ferromagnetism in Mn doped ZnO which is due to localised magnetic moment mediated by free charge carriers. The partially filled *f*-orbital of rare earth carries magnetic moment, which may take part in magnetic coupling such as transition metals with partially filled *d*-orbital[146]. The ferromagnetic behaviour has been observed for different rare earth doped ZnO such as Ce doped ZnO, Nd doped ZnO, Gd doped ZnO, Tb doped ZnO, Er doped ZnO, Eu doped

ZnO[147-148]. The occurrence of RTFM in lanthanides doped ZnO can be attributed to oxygen defect and high magnetic moment of lanthanides ions (such as Tb: 9μB) [149].

The ionic radius and charge of europium (0.95Å) is significantly larger than zinc (0.60Å for IV coordination). Therefore, it is challenging task to dope europium in zinc oxide without affecting ZnO crystal structure. In case of europium doped zinc oxide, charge compensation has been done by local defect which leads to deformation of crystal structure. Thus, a charge compensating material is required for stable compound. The suitable materials for charge compensator are alkali metals (Na, K, Li) etc. It has been observed that Li is most appropriate material as a charge compensator. Enhancement in luminescence property of doped ZnO has been achieved by addition of Li co-dopant [20]. Zinc oxide is *n*-type semiconductor. Most of the study on Li doped ZnO are focussed to make it *p*-type material. It has been observed that Li concentration remarkably affect the optical, magnetic and electrical properties of zinc oxide [150]. The exact mechanism and role of Li on optical and magnetic properties of europium doped ZnO are still a topic of discussion.

In this study, we have successfully prepared europium doped ZnO co-doped with different Li concentration (0.25-1.0%) without any impurity phase formation. We are focussed to maintain the crystal structure of ZnO and interested to enhance its optical and magnetic properties without increasing Eu doping concentration. In order to shed more light on correlation between structural change with optical and magnetic properties, we have investigated the local structure with the help of XAS analysis. We found enhancement in luminescence and ferromagnetism without impurity phase. This may prompt the advancement in magneto-optical and optoelectronics devices. Enhanced ferromagnetism by addition of Li in europium doped ZnO has not been reported earlier. This work explains the role of Li concentration on optical and magnetic property of europium doped ZnO nanoparticles prepared by sol-gel method.

5.2. EXPERIMENTAL PROCEDURE

5.2.1 Materials

Zinc acetate dehydrate [$Zn(CH_3CO_2)_2.2H_2O$], europium(III) acetate hydrate [$Eu(OOCCH_3)_3.xH_2O$], lithium acetate [$CH_3.COOLi.2H_2O$] and isopropyl alcohol have been taken as starting materials without any further purifications. Urea has been used for proper burning of samples.

5.2.2 Preparation of Samples

Zinc oxide and (Eu, Li) co-doped zinc oxide nanoparticles were synthesized by sol gel route using high purity analytical grade acetates of zinc, europium and lithium, without any further purification. We have prepared pure zinc oxide, Eu (1%) doped zinc oxide and Eu (1%) doped zinc oxide co-doped with different lithium concentration (0.25%, 0.5% and 1.0%). The compositions are indicated with code name ZnO, Eu1, Li0.25, Li0.5 and Li1.0 respectively. Briefly, for Eu (1%) doped zinc oxide nanoparticles, we dissolved stoichiometric amount of zinc acetate dehydrate in isopropyl alcohol with the help of magnetic stirring for 1 hour and the added stoichiometric amount of europium(iii) acetate hydrate with stirring 2 hours for complete dissolution of precursor. Moreover, urea was added as a burning agent, and then the resultant solution was stirred until the gel formation. The temperature and rpm was maintained at 80^0C and 1200 rpm respectively, throughout the process of sample preparation. The obtained gel was heated at 500^0C for 30 min followed by sintering at 600^0C for 2 hours in pellet form to remove the impurities and crystallisation of samples. Further, for the characterisation of samples, we crushed the pellets to get powder samples.

5.2.3 Characterisations

We have confirmed proper phase formation of synthesized samples using Rigaku-MiniFlex-II DESKTOP powder X-ray diffractometer with Cu K_α radiation (λ=

1.54 Å) at 30 kV and 15mA. The diffraction patterns were recorded over the range $20^o \leq 2\theta \leq 90^o$ with a step size of 0.02º. TGA and DSC analysis has been done by METTLER TOLEDO Japan in nitrogen atmosphere. The TEM images have been collected with TECNAI G^2 200kV (FEI) Transmission Electron Microscope to investigate morphology and particle sizes of samples. EDS analysis has been carried out to confirm presence of all elements in the samples using OXFORD Instrument SEM EVO 18 Research. X-ray photoelectron spectrum (XPS) has been recorded with an X-ray photoelectron spectroscopy setup (AMICUS, Kratos Analytical, A Shimadzu Group Company) using monochromatic MgK_α (1253.6eV) source. Raman spectra ranging from 100 to 1300 cm^{-1} have been collected with a LABRAM-HR dispersive Raman Spectrometer. The optical absorption spectra of the samples have been recorded in the range of 200-800nm with the help of JASCO V750 UV-Vis spectrophotometer. Photoluminescence spectra have been measured by Horiba Fluorolog-3 spectrophotometer equipped with 450w xenon flash lamp. The information about functional groups present in the samples has been obtained by Fourier transform infrared (FTIR-8400S) spectrophotometer. The magnetic properties have been investigated using Quantum Design MPMS-3 magnetometer in temperature range 5-300 K. The local structure has been investigated by XAS measurement at Raja Ramanna Centre for Advanced Technology (RRCAT), Indore, India, with the Energy-Scanning EXAFS beamline (BL-9) in fluorescence mode at the Indus-2 Synchrotron Source (2.5GeV, 200mA).

5.3. RESULTS AND DISCUSSION

5.3.1 Thermal Analysis

The thermal properties of Eu (1%) doped zinc oxide have been deliberated by differential scanning calorimetry (DSC) and thermo gravimetric analysis (TGA). The sample burnt at 500^0C for 30 minute has been used for thermal analysis. The europium

doped ZnO nanoparticles has been heated in an alumina pan up to 1000^0C at the rate of 10^0C/min in nitrogen atmosphere. The DSC plot shown in Figure 5.1 reveals two main exothermic peaks appeared at 599^0C and 634^0C. The TGA curve shown in Figure 5.1 indicates maximum weight loss (37%) occurred in the region of 426^0C to 678^0C. The observed weight loss can be attributed to decomposition of burning agent. The strong exothermic peak also lies within this temperature range, which indicates decomposition of fuel. After loss of burning agent from the precursor, the gradual formation of zinc oxide pure phase might also take place. The weight loss process approximately ceased after 680^0C and the stable residue that extends to 1000^0C can be ascribed to crystallisation of ZnO:Eu nanoparticles.

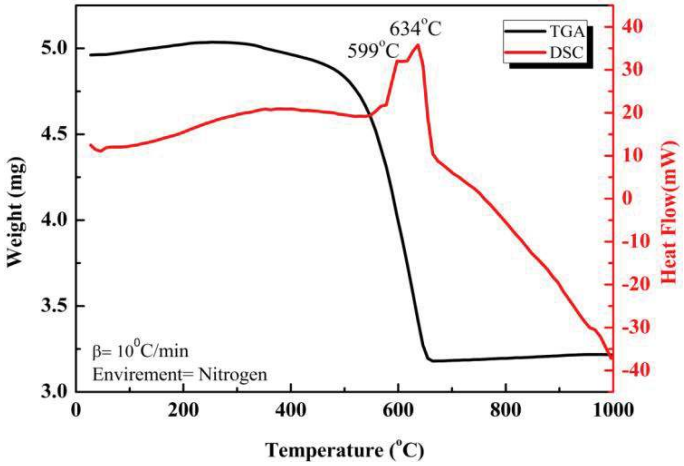

Figure 5.1: TGA- DSC of ZnO:Eu(1%) nanoparticles.

5.3.2 Structural Analysis

Figure 5.2(a) depicts the rietveld refined XRD spectra of pure and doped zinc oxide nanoparticles sintered at 600^0C. The observed peaks of all samples are found to be in good agreement with standard Bragg's positions of hexagonal wurtzite crystal structure of pure zinc oxide nanoparticles (PDF: 792205). The sharp and intense peaks ascertain crystalline nature of samples and no impurity phase has been observed within the detection limit of instrument. The presence of all standard peaks in doped zinc oxide

samples without any additional crystalline phase such as Eu_2O_3, confirms that doped zinc oxide exhibits same crystal structure and belongs to $P6_3mc$ space group. The XRD analysis indicates that europium behaves as substitutional dopant in zinc oxide without changing its crystal structure. The lattice parameters of all samples have been calculated by rietveld refinement of XRD data and listed in Table 5.1. Figure 5.2(b) indicates that lattice parameters *a* and *c* increases with europium doping and lithium co-doping up to 0.5%, after that there is slight decrease in lattice parameter for Li1.0% co-doping. The increase in lattice parameters may be due to expansion of lattice by substitution of Eu at Zn site of zinc oxide crystal structure. Since Eu (0.95Å) have higher ionic radius than Zn (0.60Å), therefore substitution of europium at Zn site causes lattice expansion. The lattice expansion in lithium co-doped samples (Li0.25 and Li0.5) may be due to incorporation of lithium at interstitial site. Li^{+} ions have approximately same value of ionic radius (0.59Å) as compared to Zn^{+2} (0.60Å) ions. When lithium concentration increases (Li1.0), it takes substitutional position which causes decrease in lattice parameters[151]. For ideal HCP structure $a = b \neq c$ and c/a =1.633 the ratio of lattice parameters (c/a) indicate distortion from ideal crystal structure. We observed small variation in c/a ratio by europium and lithium doping. This indicates substitution of dopant at Zn site and shift of crystal structure towards higher symmetry. The volume of unit cell has been calculated using Equation 4.1. The calculated values of unit cell volume have been tabulated in Table 5.1. The variation in unit cell volume can be justified by change in lattice parameters. Atomic packing fraction has been calculated using Equation 4.2. The values of APF are listed in Table 5.1 .The observed value of APF is approximately 75%, while for bulk zinc oxide value of APF is 74%. The observed slightly large APF value may be due to size effect in nanoparticles samples. It should be pointed out that value of APF for doped zinc oxides slightly increases, which

indicates incorporation of dopant in the host lattice. The crystallite size has been calculated using Scherer's formula [142] (Equation 3.1).

The average crystallite size has been calculated by taking average of crystallite sizes corresponding to each Bragg's angles and listed in Table 5.1. The inset of Figure 5.2 shows variation of crystallite size with composition. The average crystallite size decreases significantly for Eu(1%) doping because europium ions restrain the grain growth. The decrease in crystallite size by europium doping has been reported in literature [139,152]. The variation in crystallite size depends upon growth of ZnO grains. The moment and diffusion of Zn^{+2} ions are responsible for growth of ZnO grains. Small amount of lithium ions act as charge compensator and increase electrical conductivity due to presence at interstitial position. It favours the grain growth. Therefore, a slight increase in crystallite size has been observed. The doping of higher lithium concentration (1%) causes substitution of Li at Zn site of ZnO crystal structure, which decrease the lattice parameter as well as crystallite size. The formations of electrically inactive Li_{Zn}–Li_I pair are also responsible for decrease in crystallite size [153].

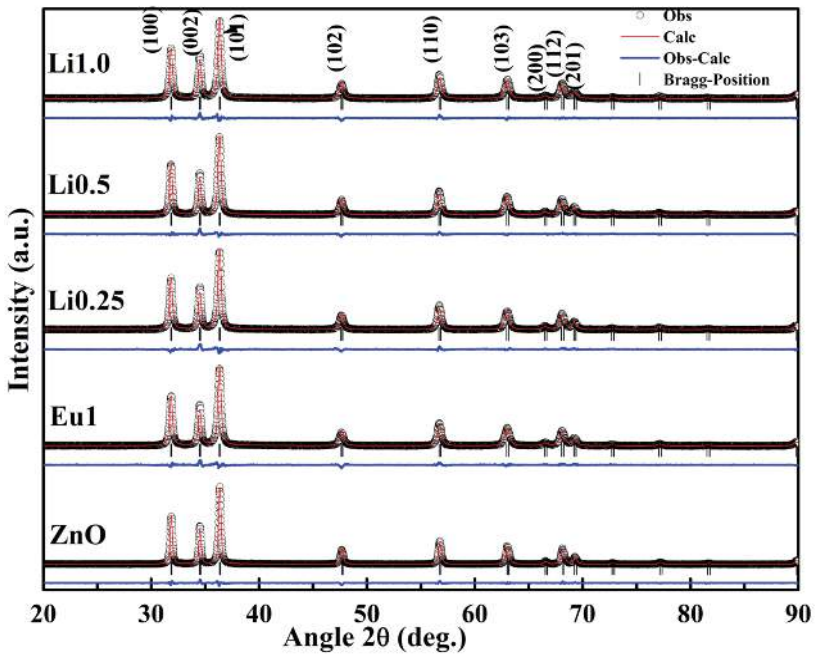

Figure 5.2(a): Rietveld refine XRD patterns of pure and doped zinc oxide nanoparticles.

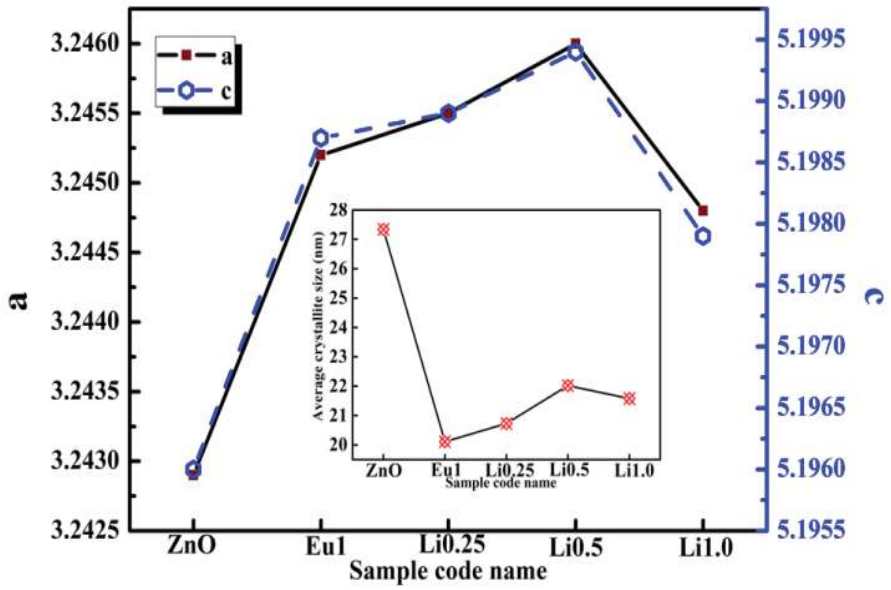

Figure 5.2(b): The variation of lattice parameters (*a* and *c*) with compositions. Inset shows change in crystallite size.

Table 5.1: The Lattice Parameter, Crystallite Size, Cell Volume and Atomic Packing Fraction of the Samples.

Sample code name	Lattice parameter		Ave. crystallite size(nm)	Cell volume $(Å)^3$	APF
	a(Å)	c(Å)			
Zn	3.2429	5.1959	27.34	47.3231	0.7550
Eu1	3.2452	5.1987	20.11	47.4148	0.75515
Li0.25	3.2455	5.1989	20.73	47.4245	0.75519
Li0.5	3.2460	5.1994	22.02	47.4431	0.75523
Li1.0	3.2448	5.1979	21.58	47.3952	0.75517

5.3.3 Morphological and Elemental Analysis

The TEM analysis has been employed to gain insight on morphological aspect of the particles. The elemental analysis has been done with the help of EDS. TEM image of zinc oxide, Eu(1%) doped zinc oxide and Eu(1%) doped zinc oxide co-doped with Li(1%) are shown in Figure 5.3(a), 5.3(b) and 5.3(c) respectively. This investigation ascertains that all samples are nearly spherical in shape and smooth in surface. No

particular morphological change has been observed due to europium and lithium doping. The nanoparticles shown in Figures are stuck together and look like a cluster. This type of image formation may be attributed to electrostatic force as well as an artefact of drying on an aqueous suspension. The inset of Figure 5.3(a), 5.3(b) and 5.3(c) represents the particle size distribution in the range of 10 to 100 nm. The average particle size of zinc oxide, Eu(1%) doped zinc oxide and Eu(1%) doped zinc oxide co-doped with Li(1%) are 65nm, 49nm and 37nm respectively. The average particle size of all the samples has been estimated by considering large number of particles. Maximum particle in zinc oxide lies within 50-60 nm range, while in case of ZnO:Eu(1%) and ZnO:Eu:Li(1%) most of the particles are in 30-40 nm range. These results demonstrate that particle size decreases due to doping of europium and lithium, which are consistent with our XRD observations. The selected area electron diffraction (SAED) pattern for pure zinc oxide has been shown in Figure 5.3(d). Similar type of diffraction pattern has been obtained for other samples. The ring formation confirms the polycrystalline nature of all samples under investigation.

In addition to morphological analysis, we have performed elemental analysis of pure and europium doped zinc oxide to ascertain the presence of all elements in the samples. EDS spectra represent qualitative and quantitative analysis of entire elements present in the samples. Elemental mapping for distribution and relative proportion of Eu(1%) doped zinc oxide over the scanned area is shown in Figure 5.4. The pie chart delineates the existence of all elements in appropriate proportion. We could not confirm the presence of lithium with EDS analysis due to limitation of instrument. Further, XPS characterisation has been carried out, which ascertains the existence of lithium.

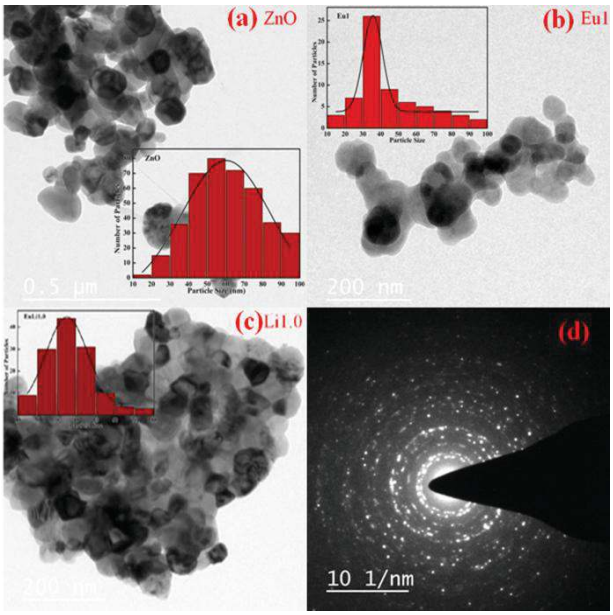

Figure 5.3: TEM image and particle size distribution of **(a)** ZnO **(b)** ZnO:Eu(1%) **(c)** ZnO:Eu(1%):Li(1%) nanoparticles. **(d)** SAED pattern of zinc oxide nanoparticles.

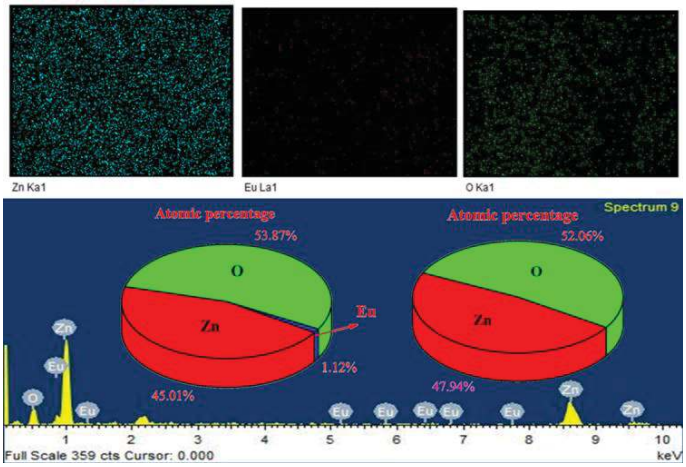

Figure 5.4: EDS spectra, elemental mapping of ZnO:Eu and atomic percentage distribution of ZnO and ZnO:Eu nanoparticles.

5.3.4 Raman Analysis

The structural and vibrational properties of all samples have been investigated with help of Raman spectra. The primitive cell of zinc oxide consists of four atoms. The 12 phonon branches related to zinc oxide atom can be divided in to nine

optical and three acoustic branches [154]. The optical phonon irreducible representation is given by Equation 4.3. Raman spectra of zinc oxide and doped zinc oxides have been depicted in Figure 5.5(a). The analysis confirms that all prominent peaks observed in ZnO are also present in doped ZnO samples without any shift in wave number. The values of vibration frequencies are same in all samples. The peaks at the same wave number ascertain that doped samples preserve the crystal structure of host zinc oxide. The peaks observed at 101, 333, and 440 cm^{-1} corresponds to E_2^{low}, E_2^{high}- E_2^{low} and E_2^{high} respectively. Figure 5.5(b) shows variation in peak intensity of E_2^{low}, which is related to motion of Zn sub-lattice. The change in intensity can be attributed to small lattice distortion, defects and change in crystalline quality [155] and confirms substitution of dopant at Zn site. The vibrational frequency observed at 586 cm^{-1} indicates E_1 (LO). This originates due to host defects such as oxygen vacancies and Zn interstitials [156]. The broad peak at 1157 cm^{-1} correspond to combined effect of $2A_1$ (LO) and $2E_1$ (LO) modes at the point of brillouin zone. The absence of any extra vibrational modes indicates that all samples same crystal structure without any deformation. The Raman analysis results are well consistent with those of XRD results.

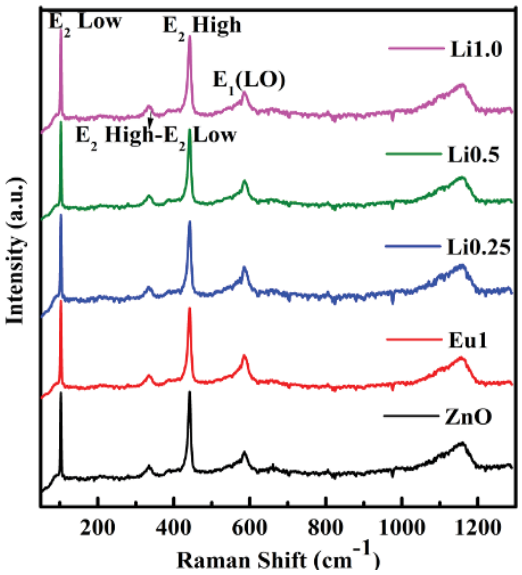

Figure 5.5(a): Raman spectra of pure and doped zinc oxide.

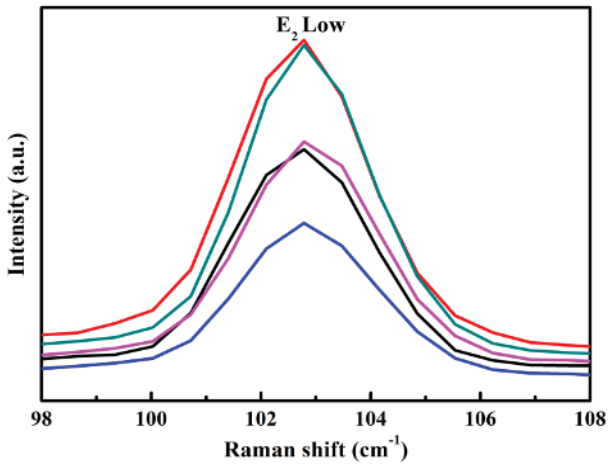

Figure 5.5(b): Intensity variation of E_2 Low in Raman spectra of pure and doped ZnO

5.3.5 FTIR Analysis

The FTIR analysis has been used to obtain information about functional group, inter or intra molecular interaction and vibrational modes due to Zn-O bond. The room temperature FTIR spectra has been recorded in the range of 400-4000 cm^{-1} and shown in Figure 5.6. All the observed wave numbers are assigned and tabulated in Table 5.2. The broad peak at 595-616 cm^{-1} for pure and doped zinc oxide corresponds to Zn-O stretching. This confirms the wurtzite structure formation of samples [103]. The slight variation in Zn-O stretching related peak indicates small lattice distortion due to dopant, but crystal structure has been maintained in all samples under investigation. The absorption peaks of Zn-O are shifted towards higher wavelength in lithium co-doped samples. This behaviour can be attributed to doping of lithium ions (0.59Å) in the host lattice. The absorption peak in the range of 862 - 872 cm^{-1} indicates weak vibration of Zn-O stretching. The peaks at 1503 cm^{-1} and 1514 cm^{-1} can be assigned as stretching of C=O, while 2348 cm^{-1} and 3429 cm^{-1} represent CO_2 molecule in the air and O-H stretching respectively. The observed peak at 1910 cm^{-1} can be attributed to presence of carbonyl ligand [157]. Thus, results of FTIR, XRD and Raman analysis authenticate the substitution of dopant in ZnO crystal structure without any impurity phase formation.

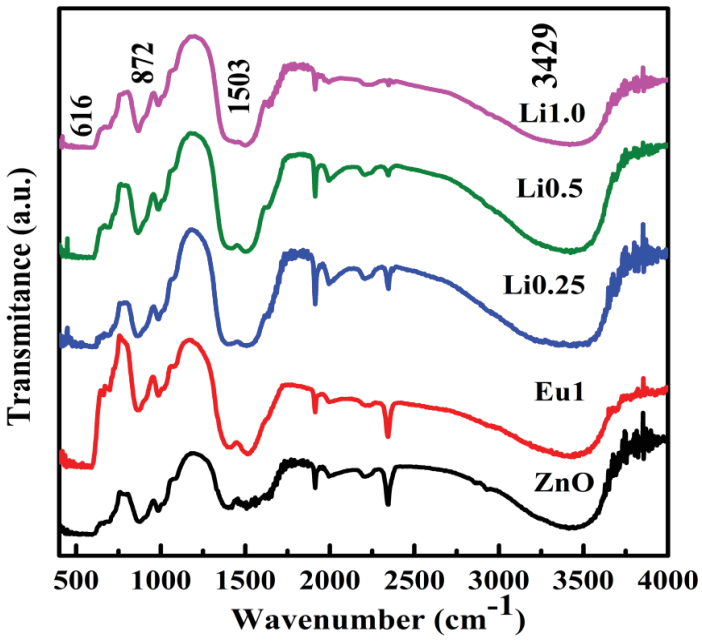

Figure 5.6: FTIR spectra of pure and doped zinc oxide nanoparticles.

Table 5.2: FTIR Peak Assignments of Pure and Doped Zinc Oxide.

Wave-numbers (cm^{-1})					Assignments
Zn	Eu1	Li0.25	Li0.5	Li1.0	
605	595	616	616	616	Zn-O stretching
872	862	862	862	872	weak vibration of ZnO
990	980	990	990	990	O-H asymmetric stretching
1397	1408	1408	1408	1408	symmetric stretching of C=O
1503	1514	1514	1503	1503	Asymmetric stretching of C=O
1910	1910	1910	1910	1910	carbonyl ligand
2348	2348	2348	2348	2348	Co_2 molecule in Air
3429	3418	3429	3429	3429	O-H stretching

5.3.6 XPS Analysis

The XPS studies have been carried out to examine the extended role of atoms present at interstitial and substitutional position that affect optical and magnetic properties of samples. The XPS survey spectra of pure ZnO, ZnO:Eu(1%) and ZnO:Eu:Li(1%) are depicted in Figure 5.7(a). These XPS survey spectra exhibit all prominent peaks of zinc, oxygen and carbon. The binding energy of C 1s peak at 284.6eV has been used for calibration of observed peaks. The XPS analysis confirms the presence of Zn, O and Li element in the samples. Europium could not be detected. It may be due to absence of Eu on the surface during characterisation. The Zn 2p core level XPS spectra exhibit two peaks at 1047eV and 1024eV corresponding to $2p_{1/2}$ and $2p_{3/2}$ respectively [158] (shown in Figure 5.7(b)). A small shift in peak position of $2p_{1/2}$ and $2p_{3/2}$ corresponding to ZnO:Eu(1%) and ZnO:Eu:Li(1%) have been observed. The shift in binding energy of Zn 2p core level may be attributed to combined effect of charge redistribution in process of chemical interaction and final state effect of photoemission process. The latter case is more effective when cluster size approx 5nm [159]. During electron hole recombination, screening effect of hole caused change in kinetic energy of out-going electron. The binding energy position of core level Zn 2p in XPS spectra concluded that Zn atoms are in +2 oxidation state.

The XPS spectra of oxygen core level 1s is depicted in Figure 5.8(a, b and c). The O1s spectra are fitted by two peaks. The observed peaks at 533eV and 535eV can be interpreted as oxygen ion of Zn-O bonding and defect oxygen or oxygen vacancies respectively [151]. The defect oxygen peak of O1s increases in europium doped sample and maximum in Li(1%) co-doped sample. Thus, XPS analysis confirms the increase in oxygen vacancy with doping of Eu and Li, this may be responsible for change in optical and magnetic properties of samples. The XPS scan performed to analyse Li atoms are

depicted in Figure 5.8(d). The higher binding energy peak centred at 57eV can be ascribed as Li substitutional (Li_{Zn}) and indicate Li-O bonds. The lower binding energy peak centred at 53eV cab be assigned to Li interstitial and this arises due to Li_I defect [151]. The spectra confirm the presence of Li_{Zn} and Li_I. The presence of Li at different position (interstitial/substitutional) can play an important role in defect mediated ferromagnetism of zinc oxide.

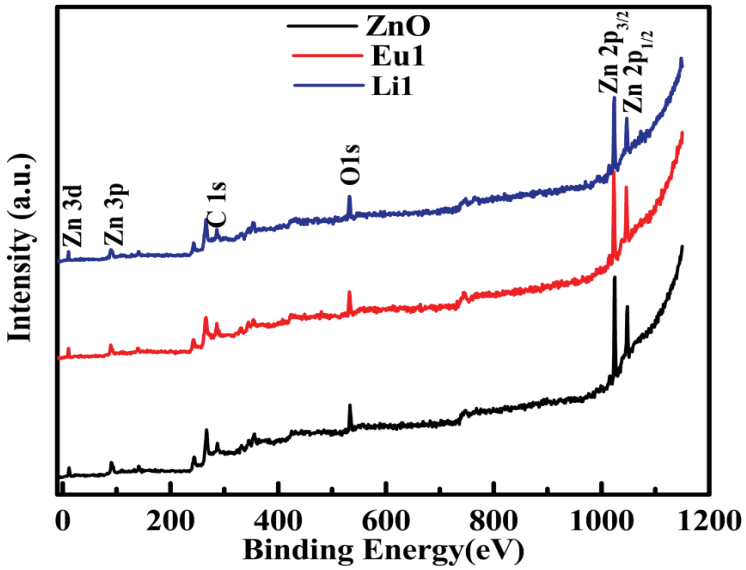

Figure 5.7(a): XPS survey of ZnO, ZnO:Eu(1%), ZnO:Eu(1%):Li(1%) nanoparticles.

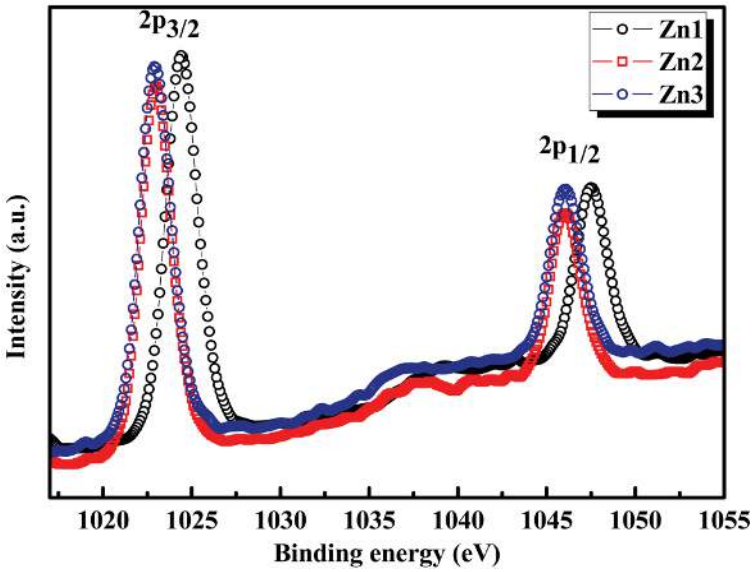

Figure 5.7(b): Zn 2p core level XPS spectra.

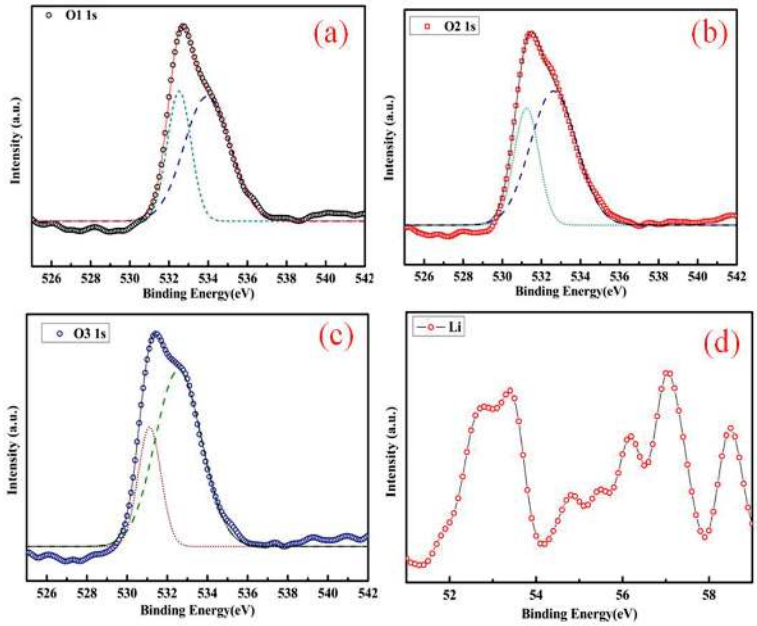

Figure 5.8: XPS spectra oxygen core level 1s of (a) ZnO (b) ZnO:Eu, (c) ZnO:Eu:Li(1%) and (d) XPS spectra of Li.

5.3.7 X-Ray Absorption Spectroscopy (XAS)

In the present study, we have performed X-ray absorption spectroscopy measurements (consisting of both X-ray Absorption Near Edge Structure or XANES and Extended X-ray Absorption Fine Structure or EXAFS) on (Eu and Li) co-doped ZnO to probe the local structures around Eu, and Zn ions. The XAS measurements have been carried out at the Energy-Scanning EXAFS beamline (BL-9) in fluorescence mode [160]. The XAS analysis ascertains local structure information, such as oxidation state, disorder, bond length and coordination number of elements in pure and doped zinc oxide samples.

XANES Analysis

The normalized XANES spectra at Zn K edge is shown in Figure 5.9(a). The absorption edge position is indication of the oxidation state of Zn ions in ZnO. The edge position is remained same at the energy of ZnO for Eu doped as well as (Eu, Li) co-doped sample. This means that Zn is present in +2 oxidation state in all doped sample. The XANES spectra are shown in Figure 5.9(b) at Eu L3 edge along with Eu_2O_3 standard. The

edge position clearly indicates that Eu is present as +3 oxidation state here, however the white-line intensity of Eu doped and (Eu, Li) co-doped samples is higher than the Eu_2O_3 indicating different coordination environment as compare to Eu_2O_3.

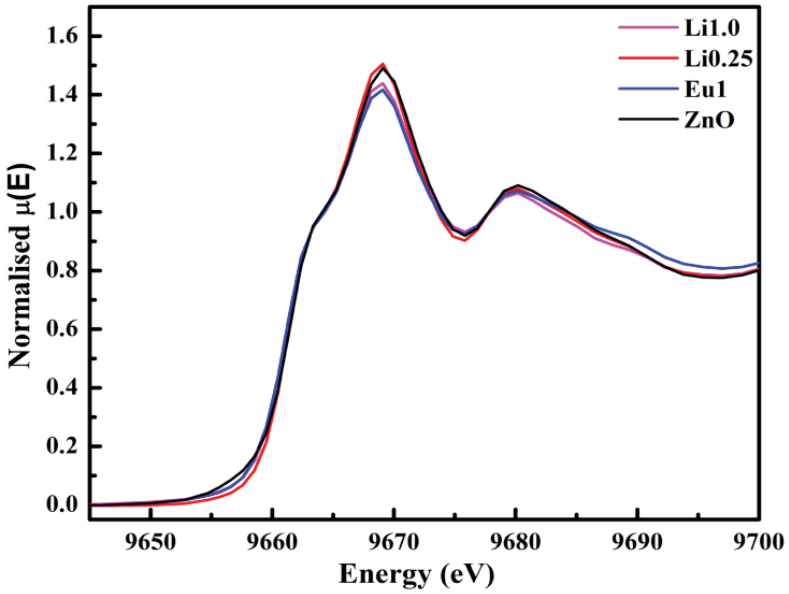

Figure 5.9(a): Normalised XANES spectra of Eu and Li co-doped ZnO measured at Zn K-edge

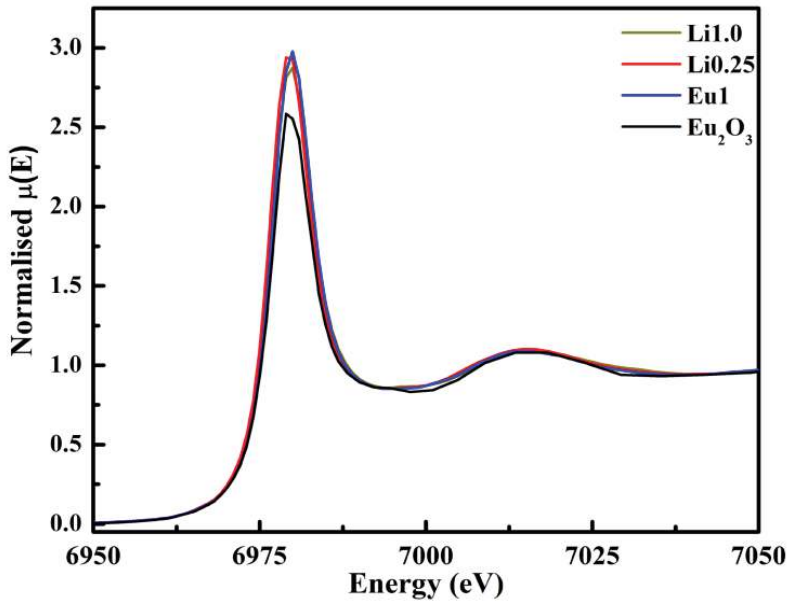

Figure 5.9(b): Normalised XANES spectra of Eu and Li co-doped ZnO measured at Eu L3-edge.

EXAFS Analysis

The normalized EXAFS spectra are shown in Figure 5.10(a) and Figure 5.10(b) at Zn K edge and Eu L3 edges respectively. In order to take care of the oscillations, we have converted the absorption spectra $\mu(E)$ to absorption function $\chi(E)$ using the relation[161]

$$\chi(E) = \frac{\mu(E) - \mu_0(E)}{\Delta\mu_0(E_0)}$$

Where, E_0 represent absorption edge energy, $\mu_0(E_0)$ is the bare atom background and $\Delta\mu_0(E_0)$ is the step in $\mu(E)$ value at the absorption edge. The wave number dependent absorption function $\chi(k)$ has been obtained from energy dependent absorption function $\chi(E)$ using the relation, $K = \sqrt{\frac{2m(E-E_0)}{\hbar^2}}$

Where, m represents mass of electron. $\chi(k)$ is weighted by k^2 to amplify the oscillation at high k and the $\chi(k)k^2$ functions are Fourier transformed in R space to generate the $\chi(R)$ versus R spectra (or the FT-EXAFS spectra) in terms of the real distances from the centre of the absorbing atom. The EXAFS data analysis has been carried out using set of EXAFS data analysis software available within IFEFFIT package [162]. This includes background reduction and Fourier transform to derive the χ(R) versus R spectra from the absorption spectra (using ATHENA software), generation of the theoretical EXAFS spectra starting from an assumed crystallographic structure and finally fitting of experimental data with the theoretical spectra using ARTEMIS software.

The Fourier transformed EXAFS spectra (χ(R) Vs R) obtained from above methodology is shown in Figure 5.10(c) at Zn K edge. The peaks obtained in Fourier transformed spectra are corresponding to the each coordination shell around the absorbing

atom. The peak shown in the Fourier transformed spectra [shown in Figure 5.10(c)] is shifted to the lower bond length side as phase correction is not included while plotting, however the fitting is done including the phase shift. The theoretical spectra are generated from the structural parameters of ZnO obtained from the XRD refinement. The bond length (R) and the disorder factor (σ^2), which is the representation of mean square displacement in the bond length, are kept as the fitting parameters during the fitting and the best fitting results are plotted in Figure 5.10(d). The first peak in ZnO at 1.5 Å is contribution of four oxygen atoms at the distance of 1.97 Å and the second peak at 2.9 Å is contribution of 12 Zn atoms at the distance of 3.21 Å. As it is shown in Figure 5.10(d), the Zn-O and Zn-Zn bond length is marginally decreasing when Eu is doped in ZnO which is further decreased for ZnO:Eu:Li(0.25%) sample, however it is start increasing for Li1.0. This decrease in the bond length can be understood as follows. The lattice constant is the side length for a hexagonal wurtzite crystal. The bond length is the distance between nearest atoms, which is different for FCC, BCC or simple cubic crystals, even if they have the same lattice constant. Typically, smaller bond lengths mean the electrons are more tightly bound to the atom, the result of APF shows an increase with dopant (Table 5.1) i.e. system is more closely packed and distance between nearest atom decreases. This leads to decrease in bond length. When Eu is substituted at Zn site, it causes lattice expansion due to higher ionic radius. The marginal decrease in bond length of Zn-O or Zn-Zn may be to preserve the crystal structure. The decrease in the bond length for Li(0.25%) compared to Eu doped ZnO may be due to the interstitial Li atoms which have smaller Zn-Li (2.70Å) bond distance and the further increase from Li(0.25%) to Li(1.0%) is due to the increase in the substitution Li sites [163]. We have observed slightly higher σ^2 for pure ZnO for Zn-O coordination shell and it decreases for Eu doped ZnO and Li(0.25%) co-doped ZnO sample, however it again start to increase for

Li(1.0%). The opposite trend of σ^2 is obtained for Zn-Zn coordination shell. The increase in the σ^2 for Zn-Zn coordination shell is obvious as the larger size of Eu atoms for Eu doped ZnO and the decrease in the σ^2 for Li(1.0%) is indication of substitution of smaller ionic radii Li^{+1} ion (0.59 Å) at Zn site [164].

The Fourier transformed EXAFS spectra at Eu L3 edge is shown in Figure 5.10(e). The first coordination peak between 1-2.5 Å is only observed and there are very weak peak at higher bond distances. This indicates highly disordered local structure around Eu sites, which will not give the significant second coordination peak. This can be understood as the ionic radii of Eu^{3+} (0.95 Å for (VI) coordination) is quite high as compared to the ionic radii of Zn^{2+} (0.60 Å for (IV) coordination) [164]. This large difference (~0.35Å) in the ionic radii will generate too much disorder in the lattice. The peak between 1-2.5Å for Eu doped ZnO is the merger of two Eu-O coordination peaks at 2.11 Å and 2.32 Å with the coordination number of 3.44 and 5.10 oxygen atoms. This spectral peak is quite different from the spectrum obtained by other reports [165-166]. The coordination shell at 2.11 Å with 3.44 oxygen atoms is may be possible due to the substitution sites of Eu, however the longer Eu-O coordination shell at 2.32 Å with 5.10 oxygen atoms is contribution from the Eu atoms at the surface [165]. *Huang et al.* prepared ZnO nanowires, which are further treated with Eu shown that the Eu ions are not replacing the Zn in the ZnO and most of the Eu atoms are at the surface [166]. They have shown that the Eu L3 edge spectrum of Eu doped ZnO clearly reproduces the Eu_2O_3 spectrum. The coordination number, bond length (R) and the disorder factor (σ^2) are kept as the fitting parameters during the fitting and the best fitting results are plotted in Figure 5.10(f). The Eu-O bond length is slightly increased for Zn:Eu:Li(0.25%) co-doped sample as compared to Eu doped ZnO, however it is further decreased for Zn:Eu:Li(1.0%). The coordination number is continuously decreasing from Eu doped ZnO to Zn:Eu:Li(0.25%)

and Zn:Eu:Li(1.0%), however the σ^2 is showing the increasing trend. The increase in the disorder factor is indication of incorporation of dopant at the lattice sites. However, decrease in the coordination number is may be due to the increase in the oxygen vacancy type defects near the dopant sites.

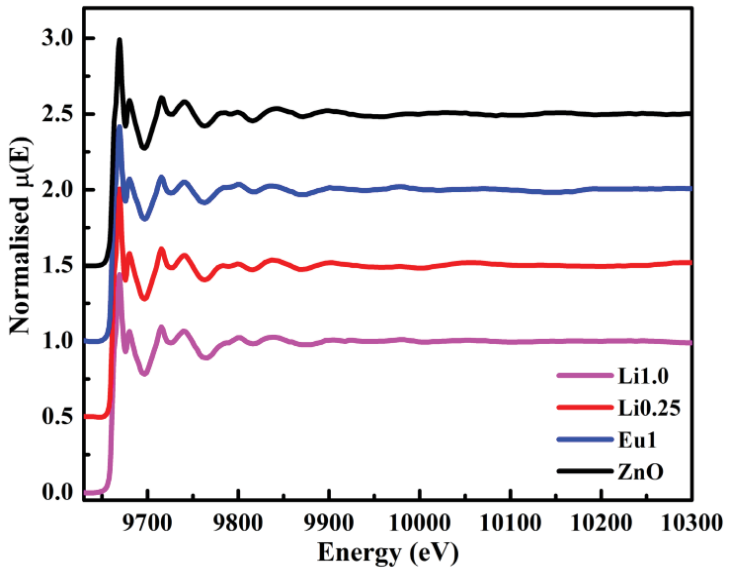

Figure 5.10(a): Normalised EXAFS spectra of Eu and Li co-doped ZnO measured at Zn K-edge.

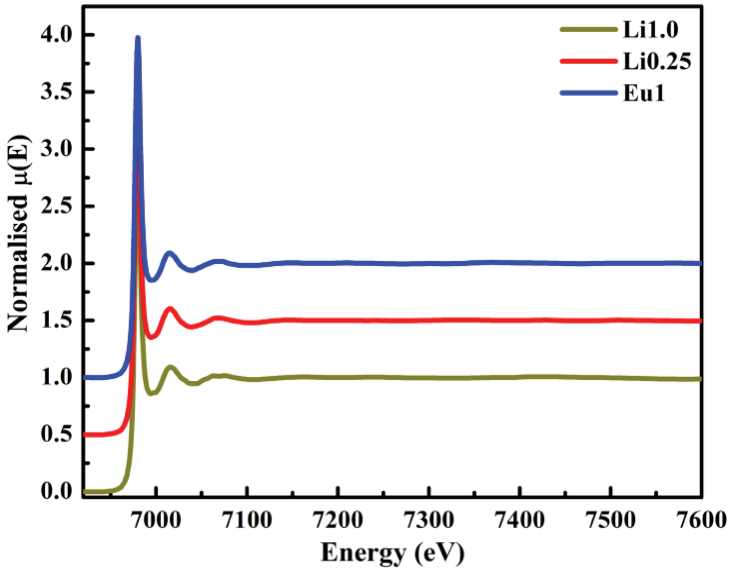

Figure 5.10(b): Normalised EXAFS spectra of Eu and Li co-doped ZnO measured at Eu L3-edge.

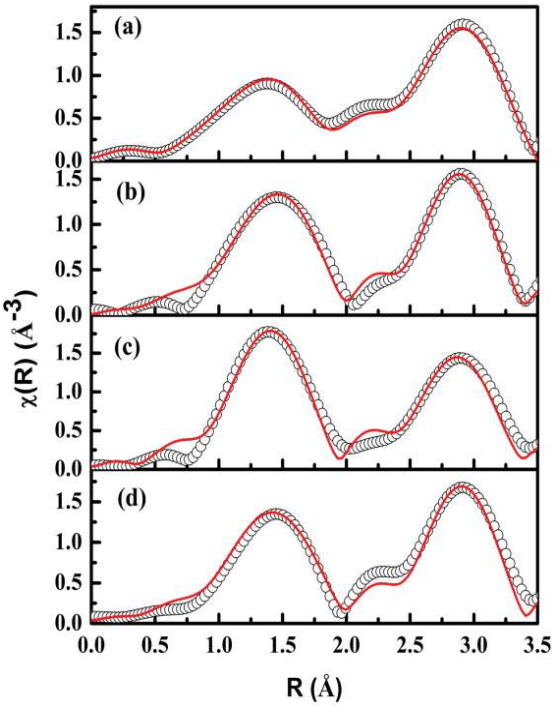

Figure 5.10(c): Fourier transformed EXAFS spectra of Eu and Li co-doped ZnO samples measured at Zn K-edge (Scatter points) alongwith the theoretical fit (Solid line): (a) ZnO, (b) ZnO:Eu(1%), (c) ZnO:Eu:Li(0.25%) and (d) ZnO:Eu:Li(1.0%).

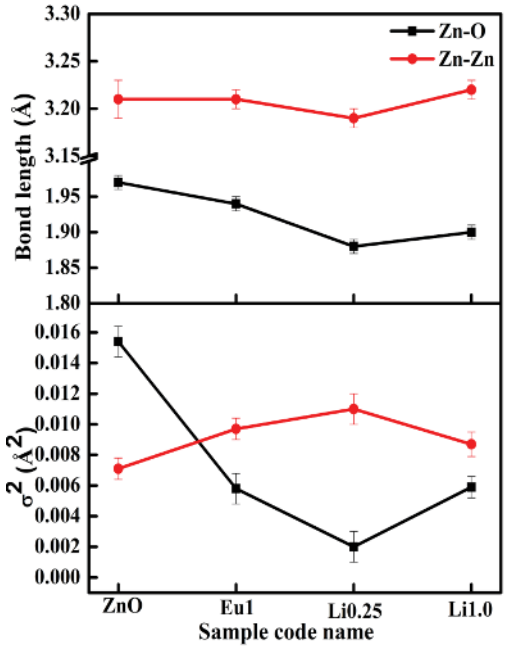

Figure 5.10(d): Variation of (top to bottom) bond length and disorder obtained from EXAFS fitting at Zn K edge.

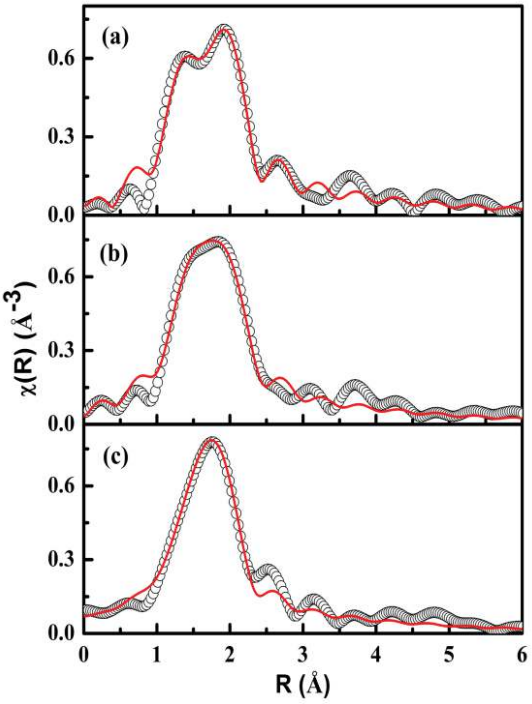

Figure 5.10(e): Fourier transformed EXAFS spectra of Eu and Li co-doped ZnO samples measured at Eu L3-edge (Scatter points) along with the theoretical fit (Solid line): (a) ZnO:Eu(1%), (b) ZnO:Eu:Li(0.25%) and (c) ZnO:Eu:Li(1.0%).

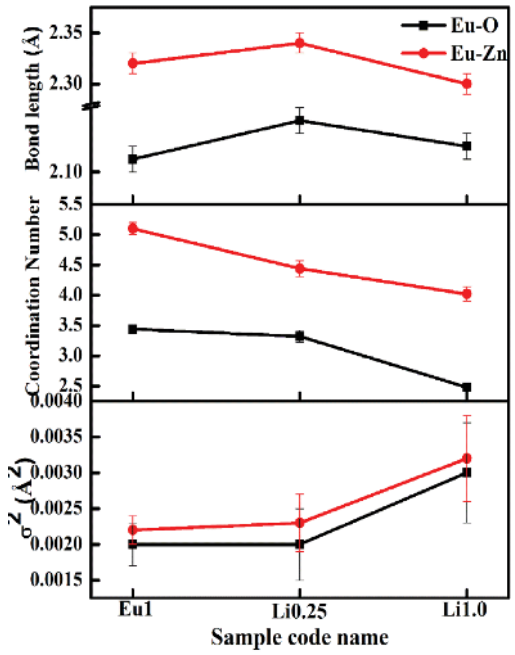

Figure 5.10(f): Variation of (top to bottom) bond length, coordination number and disorder obtained from EXAFS fitting at Eu L3 edge.

5.3.8 Absorption Study

Normalised optical absorption spectra of pure and doped zinc oxide are shown in Figure 5.11. The absorption graph indicates that very small absorption edge shift toward lower wavelength occurs due to doping. The band gap of all samples has been investigated with the help of Tauc relationship (Equation3.2). We have plotted $(\alpha h\nu)^2$ Vs $h\nu$ to determine the band gap of samples [142]. Tauc plot for pure zinc oxide is shown in Figure 5.11(inset a). It has been observed that band gap energy of europium doped zinc oxide (3.08eV) is less than pure zinc oxide (3.12eV) nanoparticles [Figure 5.11 (inset b)]. The incorporation of lithium results small increase in band gap (3.10eV) as compare to europium doped zinc oxide. Also, change in lithium concentration could not significantly affect the band gap. The band gap narrowing in europium doped zinc oxide can be attributed to charge transfer between zinc oxide valence band and 4f level of europium ions[167]. The earlier studies suggest that rare earth materials can form discreet empty energy levels below the conduction band of zinc oxide. The decrease in band gap improves the photo catalytic efficiency of europium doped zinc oxide [168]. The increase in band gap with lithium doping can be ascribed to charge compensation phenomenon. The substitution of lithium in the sample reduces the number of discrete energy level below the conduction band formed by rare earth ions, resulting small increase in band gap.

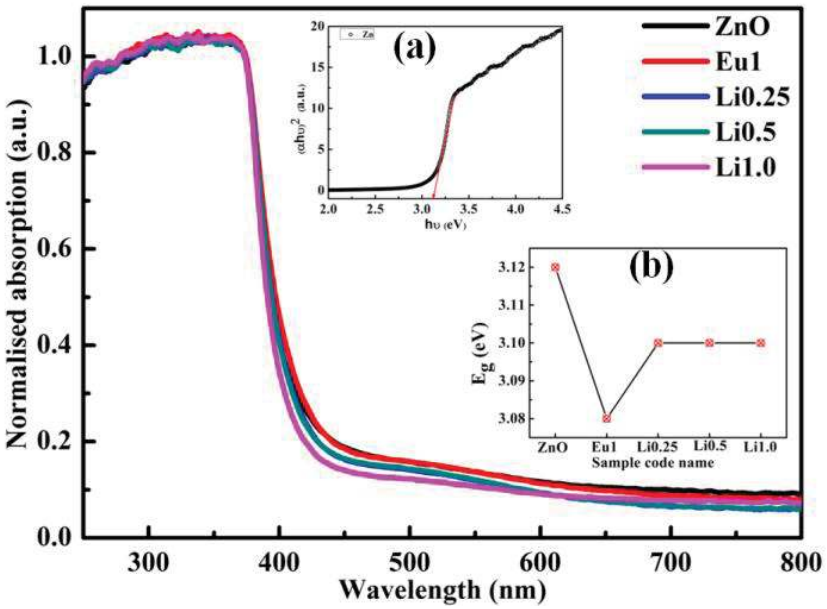

Figure 5.11: Absorption Spectra of pure and doped zinc oxide nanoparticles inset **(a)** Tauc plot of zinc oxide, **(b)** Variation of energy band gap with composition.

5.3.9 Photoluminescence Study

The room temperature photoluminescence spectra (excited with 320nm) of all samples are depicted in Figure 5.12(a). The emission study reveals the fact that all samples have wide visible luminescence centred at blue emission (450 nm). The prominent peak position of zinc oxide did not shift due incorporation of europium and lithium. A small shift in the band edge towards lower wavelength occurs due to substitution of dopant. The peaks of pure and doped zinc oxide observed at 398 nm and 411 nm can be attributed to near band edge emission (NBE) [142], which occur due to recombination of excited electron below the conduction band with hole in valance band. The slight change in NBE of doped zinc oxide may be due to increase of electron with europium substitution. The electron transition from shallow donor level to valence band originates the violet band emission at 435 nm. The blue and green emission around 465 nm and 568nm can be ascribed to defect related positively charge Zn vacancies and recombination of electron with holes trapped in singly ionised oxygen vacancies

respectively [114]. Besides emission of host, the luminescence properties of ZnO:Eu and ZnO:Eu:Li samples should be assessed in term of characteristic peak of europium ions, which are related to valance state of europium ions. The earlier study on europium doped zinc oxide suggest that broad emission centred at 530 nm is due to $4f^7$- $4f^6 5d^1$ transition of Eu^{+2} ions [169], while Eu^{+3} incorporation results intense orange/red emission around 612 nm associated to $^5D_0 \rightarrow {}^7F_2$ transition. The excitation spectra of Eu1 and Li0.25 are depicted in Figure5.12 (b). The spectra suggest that prominent excitation peaks are at 393 nm, 415 nm, and 464 nm, which correspond to $^7F_0 \rightarrow {}^5L_6$, $^7F_0 \rightarrow {}^5D_3$ and $^7F_0 \rightarrow {}^5D_2$ transition respectively [170].

The emission spectra recorded with excitation wavelength 464 nm, are shown in Figure 5.12 (c). It should be noted that there emerges peaks at 577, 591, 611, 627 and 654 nm which corresponds to $^5D_0 \rightarrow {}^7F_J$ (J=0, 1, 2, 3 and 4) respectively [170-171]. The observation perceives that orange (611 nm) and red emission (627 nm) peaks enhancement occurs with small amount of lithium co-doping. The intensity of electric dipole transition $^5D_0 \rightarrow {}^7F_2$ accredited to local symmetry of Eu^{+3} ions. This transition is very sensitive to the crystal lattice environment of Eu^{+3} ions as compared to magnetic dipole transition. The transition $^5D_0 \rightarrow {}^7F_1$ and $^5D_0 \rightarrow {}^7F_2$ suggest that Eu^{+3} ions occupy a site with inversion symmetry and inversion anti-symmetry respectively [172]. The intense electric dipole transition indicated that Eu^{+3} ions mainly occupy a site with inversion anti-symmetry in the zinc oxide. The emission enhancement in Eu^{+3} ions related peaks by different lithium concentration can be attributed to position of Li ions. The ionic radius of Li is quite smaller (0.59Å), therefore when small amount of Li (0.25%) is co-doped in ZnO:Eu, it takes interstitial position in the host lattice without disturbing the lattice structure. The EXAFS results demonstrate that Zn-O and Zn-Zn bond length for Li0.25 is less than ZnO:Eu. This indicates presence of interstitial lithium having smaller bond

distance Zn-Li (2.70Å). The increase in bond length for Li(1.0%) may be attributed to Li substation. These interstitials Li ions enhance the transition probability of rare ions. Since only few Li ions are involve in charge compensation phenomenon, therefore increase in Li concentration results substitution of Li ions at Zn^{+2} site of lattice. These substitutional Li ions originate negative as well as oxygen vacancy for charge neutralization in host. The small decrease in luminescence intensity of Eu^{+3} ions with higher Li concentration (0.5 and 1.0%) are due to distortion in the crystalline structure by oxygen vacancies. Thus, we can conclude that small amount of Li (0.25%) is suitable for luminescence enhancement of rare earth ions.

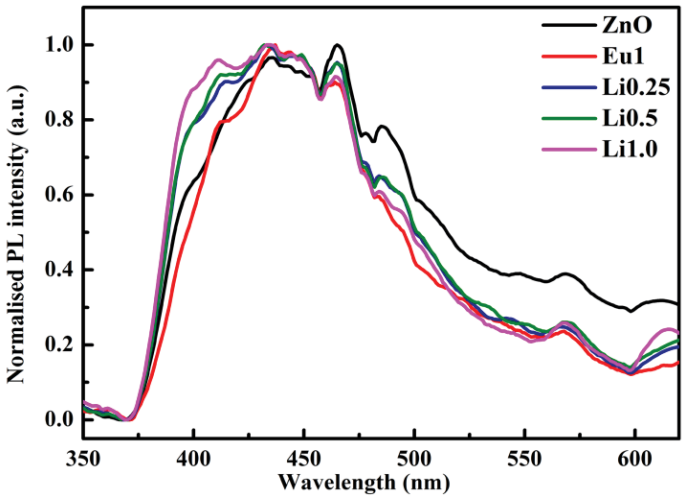

Figure 5.12(a): Photoluminescence emission spectra of samples at λ_{ex}=320 nm

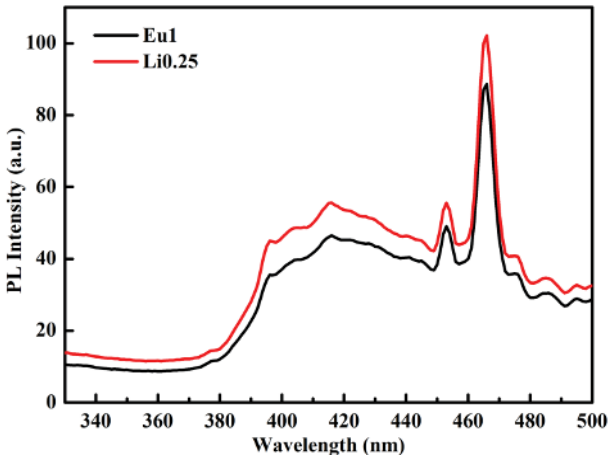

Figure 5.12(b): Photoluminescence excitation spectra of doped ZnO at λ_{em}=610 nm.

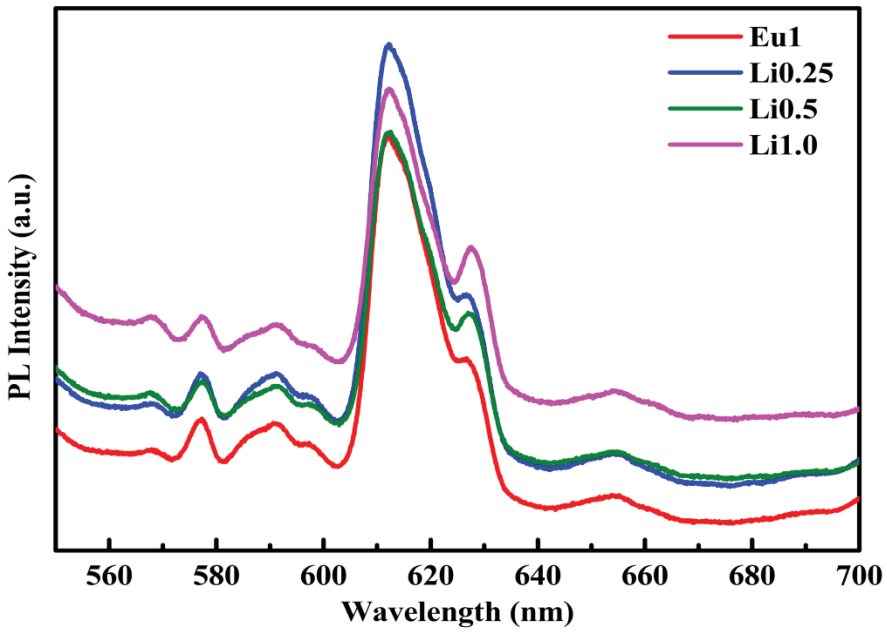

Figure 5.12(c): Photoluminescence emission spectra of samples at λ_{ex}=464 nm

5.3.10 Magnetic Property

The magnetic properties of samples have been investigated with the help of vibrating sample measurement (VSM) system. The observation ascertains presence of RTFM in all samples under investigation. Figure 5.13(a) depicts room temperature magnetisation curve of pure and doped zinc oxide nanoparticles measured at 300 K with maximum applied field ±2.0T. Figure 5.13(b) indicate close scan near origin of pure zinc oxide nanoparticles, which confirms ferromagnetic behaviour. Zinc oxide also has some diamagnetic contribution at high applied field. It has been observed that ferromagnetism decreases due to europium doping and with charge compensation by small amount of lithium ions. The increase in lithium concentration results an increase in remanent magnetisation ($M_{r)}$ values. The increase in remanent magnetisation indicates that material can sustain magnetisation. The measured values of coercive field (H_c) and remanent magnetisation ($M_{r)}$ are summarised in Table 5.3. The ferromagnetic properties of DMS has been discussed with the help of diversity of theories such as sp-d exchange interaction, Ruderman-Kittel-Kasuya-Yosida (RKKY) interaction, free carrier mediated

exchange etc. Furthermore, oxygen vacancies defects have been suggested the region of RTFM origin for oxide DMS. Earlier study suggests that europium doped zinc oxide behaves like weak ferromagnetic materials [173]. The increase in europium concentration can results increase in magnetic response, but higher europium concentration causes formation of impurity phases. In the present work, we are trying to improve magnetic response with small europium concentration with the help of lithium co-doping. The ferromagnetic properties of DMS may be due to secondary phase formation. Our study on Mn doped zinc oxide and cobalt doped zinc oxide nanoparticles ascribed that defect is an important factor affecting RTFM of DMS.

The cation vacancies in the system significantly affect the magnetic property by inducing local magnetic moment as well as holes in the system. The magnetism in such system may be mediated by holes. Small amount of lithium can be easily incorporated in the host due to small ionic radius of Li^{+}(0.59Å) and present at interstitial position. The increase in lithium doping percentage results substitution of lithium at Zn site of zinc oxide crystal structure. The substitutional lithium ions stabilize cation vacancies as well as introduce holes in the system. The stabilized cation vacancies improve the ferromagnetic property of the samples. Furthermore, oxygen vacancies defect has been suggested the reason of ferromagnetism in DMS. The EXAFS and XPS analysis of ZnO:Eu(1%):Li(1%) confirms the presence of interstitial and substitutional lithium ions. The doped lithium ions are not directly involved in ferromagnetism enhancement of system. It reduces the formation energy of Zn vacancy. Lithium ions contribute in ferromagnetism by stabilizing Zn vacancies, which originate the magnetic moment. The presence of lithium at two different position, Lithium interstitial (Li_I) and lithium substitutional (Li_{Zn}) leads to an *n*-type and *p*-type semiconductor respectively. In other words, Li_I contributes electron, while Li_{Zn} increase holes in the host zinc oxide. In

addition, neither Li_I nor Li_{Zn} enhance magnetic moment directly. In lithium doped samples, ferromagnetic enhancement occurs due to stabilization of cation vacancy and other defect such as defect oxygen by lithium ions, which are magnetic. The observed results indicate that H_c and M_r values are maximum for Li(0.5%) co-doping in Eu(1%) doped ZnO nanoparticles. The coercivity values are affected by defect in the system. Therefore higher values of H_c can be attributed to maximum defect in the system, which are generated by Li_I and Li_{Zn} ions. The lowest value of H_c for Li (0.25%) co-doped sample indicate minimum defect in the system due to charge compensation phenomenon by small amount of lithium ions. XPS results indicate that oxygen vacancies are maximum for lithium co-doped samples. Figure 5.13(c) represent ZFC plot of pure and doped zinc oxide nanoparticles. An abrupt decrease in susceptibility curve corresponds to magnetic phase change. The observation indicates that all samples exhibit Curie-Weiss behaviour. ZnO:Eu(1%) sample shows some different behaviour in the region 200-300K. the similar nature of curve has been observed by *B. Yao et al.*[174]. The presence of isolated Eu ions is responsible for complicated magnetic behaviour.

In light of observed result, the existence of ferromagnetism in our sample can be explained as follows. The Rietveld refine XRD, Raman, FTIR and local structure analysis by XAS authenticate presence of single phase in all the samples. The traces of secondary phase could not observe within the detection limit of instrument. The results of XPS and increase in the disorder factor observed by EXAFS confirm the incorporation of dopant in the host lattice. However, lattice distortion take place due to incorporation of dopant in zinc oxide crystal structure. However, decrease in the coordination number is may be due to the increase in the oxygen vacancy type defects near the dopant sites. The RTFM are correlated with structural defect. The observations ascertain that secondary phase and impurity are not responsible for ferromagnetism in our samples.

XAS and XPS result pointed out that defect oxygen/oxygen vacancy increases with europium doping and maximum in ZnO:Eu(1%):Li(1%) nanoparticles. Cation vacancy improves the ferromagnetism in the system. We believe that, observed magnetism in our samples may be combined effect of stabilized cation vacancies and defect oxygen in the system.

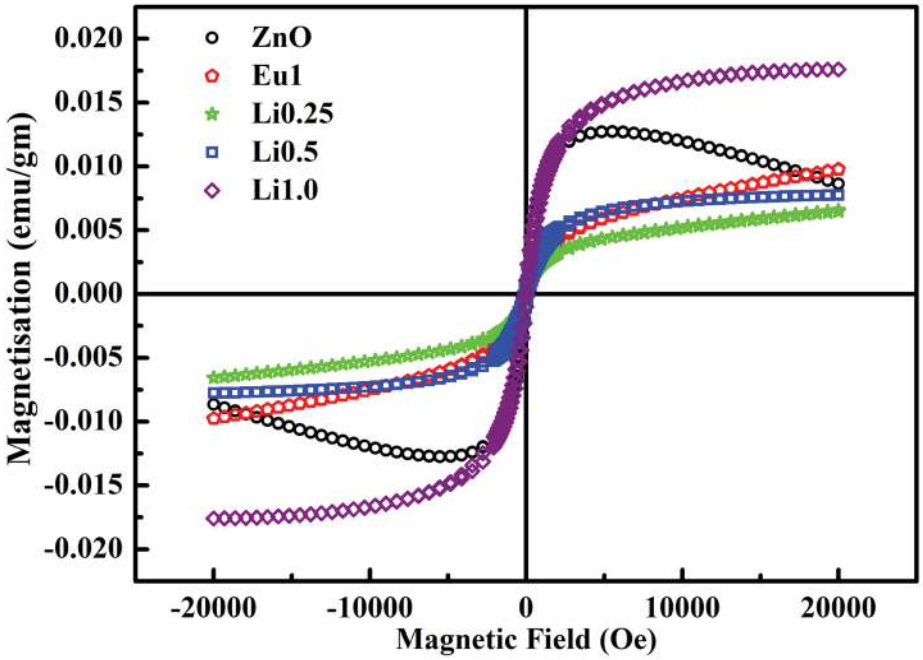

Figure 5.13(a): M-H curve of pure and doped ZnO nanoparticles at 300 K.

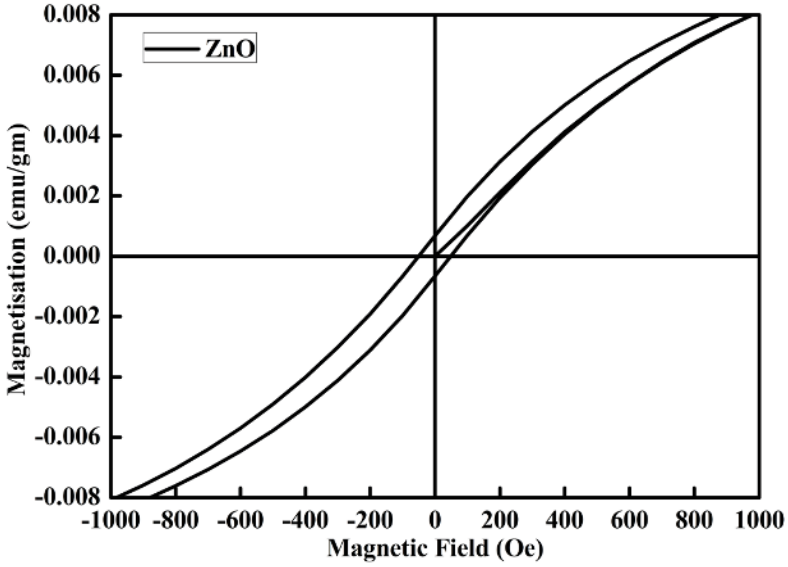

Figure 5.13(b): M-H curve of pure ZnO nanoparticles at 300 K.

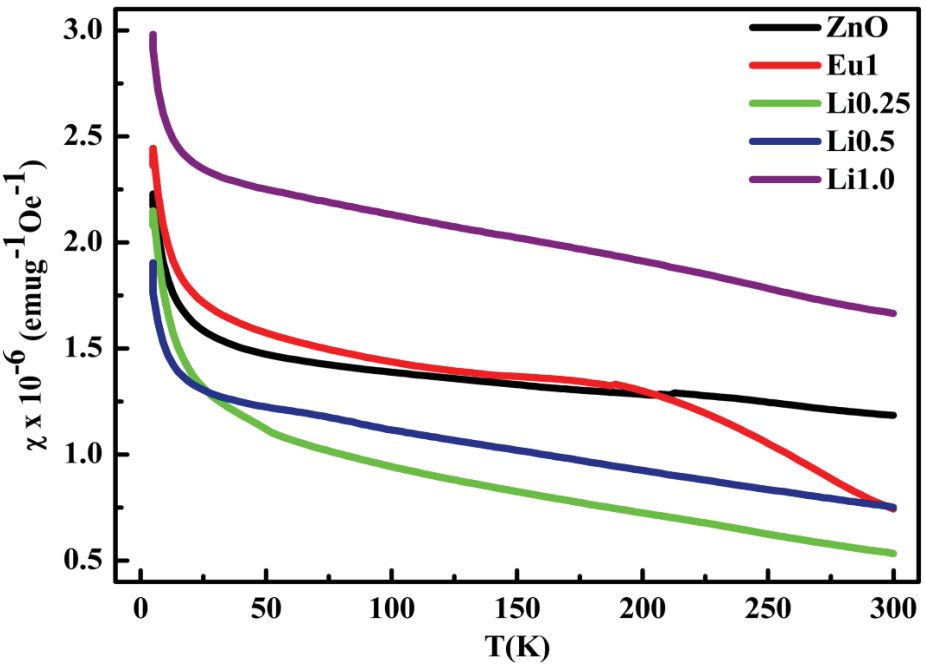

Figure 5.13(c): Susceptibility curve of pure and doped ZnO nanoparticles.

Table 5.3: The H_c and M_r Values of pure and doped ZnO.

Sample name	H_c (Oe)	M_r (emu/g)
ZnO	49.55	0.00067
Eu1	79.66	0.00044
Li0.25	45.27	0.00021
LI0.5	177.75	0.00109
Li1.0	79.05	0.00103

5.4. CONCLUSION

The present study explores the role of lithium ion concentration on structural, optical and magnetic properties of europium doped zinc oxide. All the results of structural analysis demonstrate the presence of pure phase of zinc oxide nanoparticles without any traces of side product. The XRD diffraction peaks have been assigned unambiguously to wurtzite crystal structure of zinc oxide. In addition, we have investigated local structure with the help of EXAFS analysis. The results of XANES indicate a clear signature of europium substitution and +3 oxidation state in the samples. The oxidation state measured by XPS is fully consistent with XANES measurement. The incorporation of charge compensator in small amount can improve the luminescence of the host. To ascertain this assertion, we prepare the samples with different lithium concentration (0.25-1.0%) and found enhancement in the luminescence of europium related peak with Li (0.25%) co-doping. The enhancement in ferromagnetism has been observed with higher lithium concentration (0.5-1.0%). Our study suggests that enhancement in ferromagnetism can be obtain by stabilizing cation vacancies in the system. The occurrence of enhance luminescence with ferromagnetism can trigger promising applications of such systems in magneto optical and optoelectronic devices.